chemosensors

MDPI

Article

Deep Learning Denoising for Enhanced Acetone Detection in Cavity Ring-Down Spectroscopy

Wenxuan Li [1,†], Dongxin Shi [2,†], Feifei Wang [3], Yuxiao Song [3], Yong Yang [3], Jing Sun [2,*] and Chenyu Jiang [1,2,*]

[1] School of Medicine and Information Engineering, Shandong University of Traditional Chinese Medicine, Jinan 250022, China; 2023110543@sdutcm.edu.cn
[2] Suzhou Institute of Biomedical Engineering and Technology, Chinese Academy of Sciences, Suzhou 215163, China; shidx@sibet.ac.cn
[3] Jinan Guoke Medical Technology Development Co., Ltd., Jinan 250013, China; wangff@sibet.ac.cn (F.W.); songyuxiao@sibet.ac.cn (Y.S.); yangyong@sibet.ac.cn (Y.Y.)
* Correspondence: sunj@sibet.ac.cn (J.S.); jiangcy@sibet.ac.cn (C.J.); Tel.: +86-18253121729 (J.S.); +86-13402617742 (C.J.)
† These authors contributed equally to this work.

Abstract

Cavity ring-down spectroscopy has significant potential for detecting trace volatile organic compounds, owing to its long absorption path and high sensitivity. However, in practical measurements, noise severely decreases the accuracy of decay curves and the reliability of concentration retrieval. To address this, we developed a deep learning-based denoising model called decay-upsampling FC-Net. Experimental results showed that the model improved the signal-to-noise ratio from 13.86 dB to 26.79 dB and processed a single decay curve in only 0.000207 s on average. Moreover, under high-noise conditions, it determined the ring-down time more accurately than conventional methods. This study provides an effective signal processing solution to enhance the practical reliability of Cavity ring-down spectroscopy gas detection systems.

Keywords: cavity ring-down spectroscopy; acetone concentration detection; signal denoising; deep learning; neural network filtering algorithm

1. Introduction

Cavity ring-down spectroscopy (CRDS) [1] generates exceptionally long absorption paths within a high-finesse optical cavity. Therefore, it enables highly sensitive detection of gases at ultra-low concentrations and has become a pivotal technique in trace gas analysis [2,3]. Acetone, as a widely recognized biomarker for diabetes, requires precise measurement for clinical diagnosis and monitoring. While conventional gas analysis methods such as mass spectrometry and semiconductor sensors [4–6] can be used for acetone detection, they often involve complex sample pretreatment, lengthy analysis times, or limited sensitivity. In contrast, CRDS offers not only extremely high detection sensitivity but also comprehensive advantages, including rapid response and minimal sample pretreatment. Consequently, it has broad application potential in various fields, including environmental monitoring, industrial manufacturing, and breath analysis [7,8].

However, CRDS gas detection systems are often affected by various noise sources, such as photon quantum noise, molecular absorption cross-interference [9], environmental vibration, and thermal noise from electronic components [10]. These noises distort the ring-down curve, thereby affecting accurate extraction of the ring-down time and the subsequent retrieval of the gas concentration.

Check for updates

Received: 4 March 2026
Revised: 30 March 2026
Accepted: 3 April 2026
Published: 5 April 2026

Copyright: © 2026 by the authors. Licensee MDPI, Basel, Switzerland. This article is an open access article distributed under the terms and conditions of the Creative Commons Attribution (CC BY) license.

Traditional ring-down signal processing methods [11–14] include linear/nonlinear least-squares fitting, polynomial fitting, fast Fourier transform, Savitzky–Golay filtering, and wavelet transform. Although these methods can suppress high-frequency noise to a certain extent, their effectiveness against low-frequency noise is limited. Moreover, they often rely on manual parameter tuning, which results in poor generalization capability. The limitations of these traditional methods are summarized in Table 1.

Table 1. Limitations of different algorithms for signal processing.

Algorithm	Limitations
Linear/Nonlinear Least Squares	Easily affected by the initial iteration point, leading to instability
Polynomial Fitting	Prone to overfitting and sensitive to noise
Fast Fourier Transform (FFT)	Difficulty in distinguishing noise components that share the same frequency as the signal
Savitzky–Golay Filter	Relies on manual parameter tuning, with limited generalization capability
Wavelet Transform	Effective for high-frequency noise, but struggles with low-frequency noise that is coupled with the ring-down signal
CNN-based methods	Local feature extraction limits global decay modeling; high computational cost
Transformer-based methods	Heavy resource consumption; lack of prior knowledge of decay function characteristics

In contrast to these traditional approaches, deep learning technology, which has powerful feature extraction and nonlinear mapping capabilities, has shown significant advantages in signal processing [15,16]. For instance, to address the performance degradation of traditional high-resolution line spectrum estimation methods under high noise, Jiang et al. [17] proposed an innovative framework that integrates a denoising convolutional neural network model with residual learning capability and classical algorithms. This model can directly recover nonstructured noise components from noisy signals, thereby achieving effective denoising. Furthermore, Kistenev et al. [18] adopted a deep learning architecture based on autoencoders. This model maps noisy spectral data to a highly compressed latent space in a high-dimensional nonlinear manner using an encoder. By this process, the noise in a signal is effectively suppressed, and a spectral feature representation that is discriminative against the noise can be extracted. The decoder then reconstructs the denoised signal with high fidelity based on these features. This approach avoids reliance on prior assumptions regarding signals inherent in traditional filters, and therefore, exhibits a stronger generalization capability. These findings validate the unique advantages of deep networks for feature extraction. In addition to the aforementioned models, architectures such as U-Net and transformers [19,20] have exhibited outstanding performance in denoising tasks in speech enhancement and biomedical signal processing owing to their distinctive structural advantages (e.g., skip connections and attention mechanisms). These examples highlight the broad applicability of deep learning in solving signal denoising problems.

Aiming at the continuous decay characteristics of ring-down signals, this study developed a filtering and denoising method called decay-upsampling FC-Net (DUFC) by combining upsampling with a fully connected neural network. Instead of using convolution operations suitable for local feature extraction, this method utilizes fully connected layers to directly model the global decay pattern of a signal and employs upsampling layers to achieve high-fidelity sequence reconstruction. A single-pulse CRDS experimental system was developed to validate the effectiveness of the developed method. Using standard acetone gas samples as the detection target, a dataset was constructed by collecting ring-down

curves for model training and testing. The experimental results indicated that the model can effectively separate noise from a true ring-down signal and overcome the limitations of traditional time–frequency analysis methods. The signals processed by the DUFC method, combined with nonlinear least-squares fitting, enabled high-precision extraction of the ring-down time, thereby achieving accurate inversion of the acetone gas concentration.

2. Materials and Methods

2.1. Principle of CRDS-Based Gas Detection and Background Subtraction

CRDS is based on the Lambert–Beer law [21], which expresses the attenuation of laser radiation as it propagates through a homogeneous gas. When a laser beam passes through a uniform target gas, the incident light intensity $I_0(\nu)$ and transmitted intensity $I(\nu)$ satisfy the following relationship:

$$I(\nu) = I_0(\nu)e^{-\alpha l}, \tag{1}$$

where ν is the optical frequency, α is the absorption coefficient of the target gas and l is the absorption path length.

In a CRDS system, a laser pulse is injected into an optical cavity composed of two highly reflective mirrors with reflectivity exceeding 99.9%. The light undergoes multiple reflections within the cavity, resulting in an effective optical path length of several kilometers, which significantly enhances the detection sensitivity. The intracavity light intensity decays exponentially with time as follows:

$$I(t) = I_0 e^{-t/\tau}, \tag{2}$$

where the ring-down time constant τ is related to the system parameters by

$$\tau = \frac{L}{c(1 - R + \alpha L)}, \tag{3}$$

where R denotes the reflectivity of the cavity mirrors, L is the cavity length, α is the absorption coefficient of the target gas, and c is the speed of light.

During this process, absorption of the intracavity laser pulse by the target species causes the light intensity to decay exponentially with time, forming a characteristic ring-down curve. By precisely measuring the ring-down time under vacuum, $\tau_0 = L/c(1 - R)$, and ring-down time when the cavity is filled with the sample gas, $\tau_1 = L/c(1 - R + \alpha L)$, the absorption coefficient α of the target gas can be derived as

$$\alpha = \frac{1}{c}\left(\frac{1}{\tau_1} - \frac{1}{\tau_0}\right). \tag{4}$$

According to the absorbance expression of the Lambert–Beer law, the number density n of the target gas can be calculated as

$$A = ln\left(\frac{I_0}{I_t}\right) = \alpha l = \sigma(\theta)nl, \tag{5}$$

$$n = \frac{1}{c\sigma(\theta)}\left(\frac{1}{\tau_1} - \frac{1}{\tau_0}\right), \tag{6}$$

where A is the absorbance, n is the number density and $\sigma(\theta)$ is the absorption cross-section of the target gas molecule at wavenumber θ. The total number density of the sample gas (target and carrier gases), n_a can then be obtained using the ideal gas equation of state. The ratio n/n_a corresponds to the volume fraction and thus the concentration of the target gas.

Notably, the target gas concentration derived from Equations (5) and (6) is valid only under the assumption that the sample gas, which consists of the target and carrier gases, does not interact with the laser pulse. Such ideal conditions are rarely achieved in practical measurements; therefore, a background subtraction method is required to reduce the resulting systematic errors.

The composition of exhaled human breath is complex in practical measurements. In addition to acetone, it contains water vapor, CO_2, and other volatile organic compounds, which may interfere with the absorption signal. However, for the major components (N_2, O_2, and CO_2), N_2 exhibits no absorption at 266 nm, while O_2 and CO_2 have absorption cross-sections comparable to that of acetone. Although their individual concentrations vary between breath and ambient air, their combined volume fraction remains stable (~21%). Therefore, their combined absorption contribution can be effectively removed by background subtraction. Consequently, a background subtraction method is needed to suppress this interference effectively.

The absorbance A_{breath} is obtained from the difference between the ring-down time of a breath sample τ_{breath} a ring-down time under vacuum τ_0. In reality, it includes not only the absorption of the target gas but also the absorption and scattering effects caused by other constituents in the exhaled breath.

In this study, to quantify the effect of non-acetone components on the optical pulse, the absorbance of the ambient air relative to vacuum, denoted as A_{atm}, was introduced. Accordingly, an alternating measurement sequence of vacuum–air–vacuum–breath sample was adopted to obtain the corresponding ring-down times τ_0, τ_{atm}, τ_1, and τ_{breath}. An effective absorbance primarily attributed to acetone was calculated, from which the acetone number density n can be derived based on Equation (7). The acetone volume fraction, i.e., the acetone concentration, was then obtained.

$$n = \frac{1}{c\sigma(\theta)}\left(\frac{1}{\tau_{breath}} - \frac{1}{\tau_1} - \frac{1}{\tau_{atm}} + \frac{1}{\tau_0}\right), \tag{7}$$

2.2. CRDS-Based Gas Detection System

The CRDS-based system developed in this study for measuring the acetone concentration in exhaled breath is shown in Figure 1. The system mainly consists of a laser source, a ring-down cavity, a photodetector, temperature and pressure control modules, and a signal acquisition and processing unit.

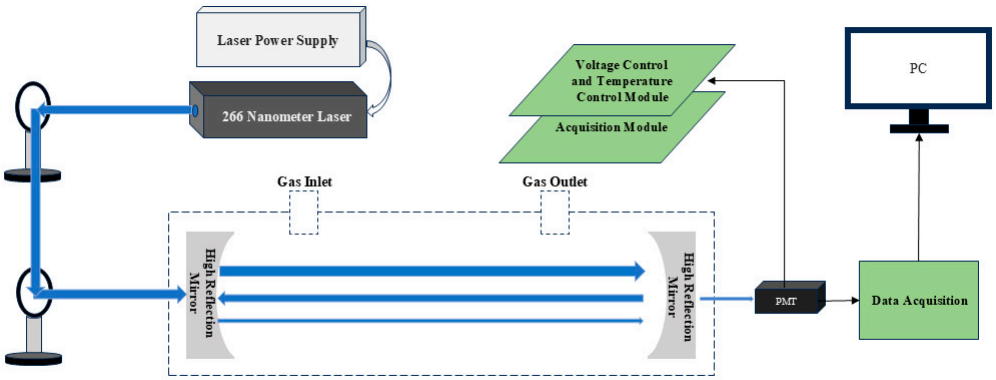

Figure 1. Schematic of the CRDS setup for human breath acetone detection.

A compact all-solid-state laser is employed as the light source to deliver pulsed laser radiation at a central wavelength of 266 nm (CryLaS GmbH, Berlin, Germany). The laser beam is first collimated using two plane mirrors and then coupled to a custom-designed optical ring-down cavity developed by our research group. The cavity is equipped with

two high-reflectivity mirrors (reflectivity $R = 99.94\%$, radius of curvature 1 m, MLD Technologies, Mountain View, CA, USA) mounted at both ends, forming a high-finesse optical resonator. This configuration enables the injected laser pulse to undergo hundreds of reflections within the cavity, thereby significantly extending the effective optical path length within a limited physical space and ensuring sufficient interaction between the optical pulse and target gas.

All experiments were conducted under ambient conditions (room temperature, atmospheric pressure). The relative humidity was maintained at approximately 40% using a dehumidifier, and a water vapor filter was installed at the gas inlet to further reduce moisture interference.

The attenuated optical signal is detected using a photodetector equipped with a 266 nm bandpass filter. The optical signal is converted into an electrical signal using a photomultiplier tube (PMT, R7400U-03, Hamamatsu Photonics, Hamamatsu, Japan) and can be directly acquired using a digital oscilloscope with a 50 Ω input impedance (Tektronix, Beaverton, OR, USA) and transmitted to a computer for further analysis. Alternatively, the signal can be digitized using an embedded data-acquisition card for subsequent signal processing and concentration retrieval.

The selection of the laser operating wavelength is critical to the measurement performance of the system described above. Although acetone exhibits characteristic absorption peaks in the infrared region, multiple components in exhaled breath, such as water vapor and carbon dioxide, also possess strong absorption in this spectral range. The dense and overlapping absorption lines in the infrared region can easily interfere with or even overwhelm the acetone signal, making accurate identification and quantification challenging. In contrast, acetone also exhibits significant absorption features in the ultraviolet region. According to the ultraviolet absorption spectrum of acetone provided by the NIST database, acetone displays a continuous absorption band in the range of 225–320 nm, with a distinct absorption peak near 266 nm. This wavelength aligns well with the output of commercially available all-solid-state ultraviolet lasers, offering convenient laser availability. Moreover, the narrow linewidth of such lasers facilitates efficient mode matching with the high-finesse optical cavity, thereby ensuring both the sensitivity and stability of the measurement system.

When determining the operating wavelength, it is also essential to evaluate the absorption effects of the major interfering components in breath. As shown in Table 2, the major components in exhaled breath (N_2, O_2, and CO_2) have a combined volume fraction similar to that in ambient air. N_2 exhibits no absorption at 266 nm, while O_2 and CO_2 have absorption cross-sections comparable to that of acetone. Although their individual concentrations vary between breath and ambient air, their combined volume fraction remains stable (~21%). Therefore, their combined absorption contribution can be effectively removed through background subtraction. Water vapor is removed by a water filtration device installed at the gas inlet. Other components, such as nitrogen, nitric oxide, carbon monoxide, and ammonia, exhibit zero or negligible absorption cross-sections at 266 nm. The absorption of isoprene and other trace gases is less than 0.5% of that of acetone, making their influence negligible.

Table 2. Absorption capacity of major components in exhaled breath at 266 nm.

Substance	Chemical Formula	Concentration in Exhaled Breath	UV Absorption Band (nm)	Absorption at 266 nm	Relative Intensity (Reference: Acetone)
Acetone	$(CH_3)_2CO$	0.49 ppmv	225–320	2.45×10^{-5}	1.000
Water	H_2O	~6%	<199	0	0
Nitrogen	N_2	78%	100–150	0	0
Oxygen	O_2	16%	250–300	2.13×10^{-5}	0.869
Carbon dioxide	CO_2	5%	105–300	5.05×10^{-5}	2.061
Nitric oxide	NO	1–20 ppbv	<230	0	0
Carbon monoxide	CO	1–10 ppmv	128–160	0	0
Ammonia	NH_3	1–1 ppmv	111–220	0	0
Isoprene	C_5H_8	50–200 ppbv	<233	1.23×10^{-7}	0.005
Other trace gases	—	0–50 ppbv	<233	$<<1.23 \times 10^{-7}$	<<0.005

2.3. Dataset Construction and Noise Modeling

In deep learning, the quality and quantity of data significantly affect the outcomes of model training. However, in practical experimental research, particularly in sensor applications, acquiring large volumes of real-world data under specific conditions is often time-consuming and expensive. To address this problem, a data simulation was conducted based on principles derived from CRDS. This approach facilitated the generation of a large and diverse set of samples for model training, validation, and optimization, thereby mitigating data scarcity, enhancing model generalizability, accelerating the training process, and reducing the experimental costs.

Equation (1) describes how the decay process of a light pulse undergoing multiple reflections within an optical cavity is governed by several factors, including the high-reflectivity mirror reflectance R, absorption coefficient of the target gas α, and absorption path length l. From a temporal perspective, these factors can be consolidated into a single constant, i.e., the ring-down time τ, thereby yielding the expression decay form given in Equation (2).

Considering effects such as the dark current of the photodetector, the decay curve may exhibit a minor vertical offset, B, as follows:

$$I = I_0 e^{-\frac{t}{\tau}} + B. \tag{8}$$

Using Equation (8), 20,000 smooth decay curves were simulated, corresponding to ring-down times ranging from 0.5 μs to 1 μs. In CRDS detection systems, the noise in a ring-down signal primarily originates from optical system interference and electronic system noise. The former includes scattering noise in the light path and interference effects within the cavity. The latter includes noise from the signal acquisition circuit, external electromagnetic interference, and shot and thermal noises from electronic components.

To characterize the dominant noise component, single-shot ring-down signals were compared with their multiple-averaged smooth counterparts. The residuals obtained by subtracting the averaged signals from the raw signals were analyzed across multiple measurements. The standard deviation of the residuals was calculated to be 0.002. Histogram analysis revealed that the residuals follow an approximately Gaussian distribution. Based on this, Gaussian noise $\varepsilon_g \sim \mathcal{N}(0, 0.002^2)$ was superimposed onto the generated decay curves to simulate the dominant noise.

In addition, to account for the uncertainties inherent in the optical system, uniform random noise $\varepsilon_u \sim \mathcal{U}(-0.001, 0.001)$ was added. This noise level corresponds to approximately 5% of the initial ring-down signal amplitude, serving as a reasonable estimate of

optical system uncertainty. This additional noise component enhances the robustness of the proposed method.

Furthermore, to realistically simulate fluctuations introduced during gas sampling and delivery in practical applications, tests were performed using a laboratory-acquired 10 ppm standard acetone gas. The standard gas was transferred from a cylinder to a fluorinated-film sample bag, which was then connected to the CRDS device to introduce the gas into the detection chamber. Multiple independent and repeated measurements were conducted under three conditions: vacuum, ambient air, and standard acetone gas. Eighteen measurements were performed for each condition. These provided a reliable data foundation for the subsequent algorithmic comparisons. To systematically evaluate the robustness of the algorithm under varying noise levels, the signal-averaging function of an oscilloscope was utilized with two configured acquisition modes: 128 and 16 averages. The former represented the baseline performance of the system under low-noise conditions, whereas the latter actively simulated a high-noise environment.

2.4. Design and Training of the DUFC Network

In the measurement process based on the CRDS system, as shown in Figure 2, a noisy raw decay curve is first processed by the DUFC neural network model to remove noise interference maximally. Subsequently, the denoised signal is fitted using the nonlinear least squares (NLS) method to extract the ring-down time τ, based on which the concentration of acetone in exhaled human breath is retrieved.

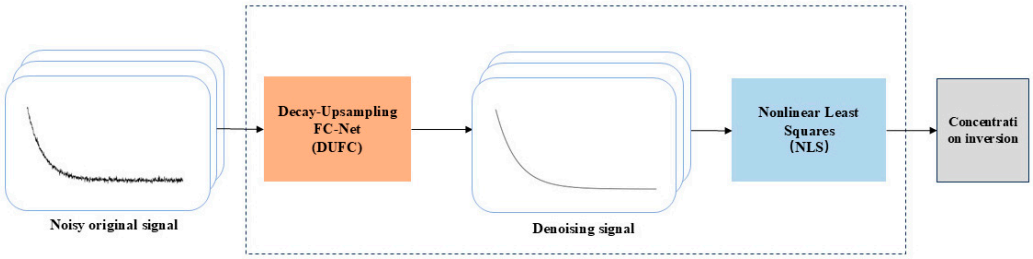

Figure 2. Flowchart of ring-down curve denoising and concentration retrieval.

As shown in Figure 3, the DUFC model consists of an alternating stack of fully connected upsampling and average pooling layers. Instead of using convolution operations suitable for local feature extraction, the core design utilizes fully connected layers to directly model the global decay pattern of a signal. The model first projects an original signal (1000 sampling points) onto a high-dimensional feature space using a fully connected layer with the rectified linear unit (ReLU) activation function to enhance the nonlinear representational capability. Subsequently, the feature map resolution is increased to 3000 sampling points via linear interpolation upsampling to enhance the temporal detail. Next, an average pooling layer with a kernel size of four is used to smooth and denoise the signal while compressing the information. Thereafter, the model maps the features back to their original length (1000 points) using another fully connected layer, followed by a smaller upsampling operation (to 2000 points) to preserve the effective information. Finally, after further pooling, denoising, and mapping using a fully connected layer, a high-fidelity denoised signal is output.

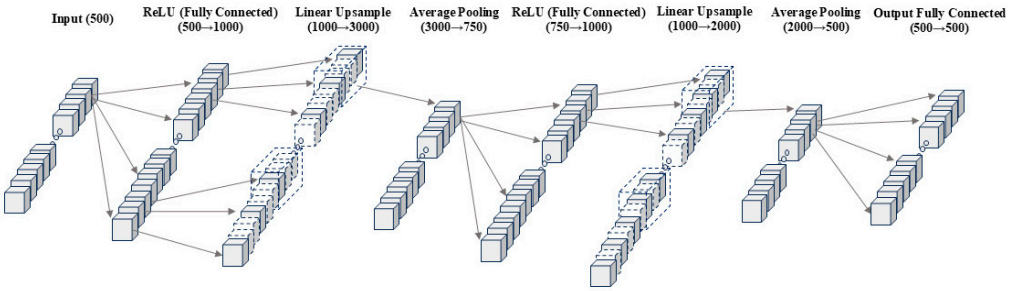

Figure 3. Architecture of the DUFC model.

The selection of hyperparameters is crucial for model training. A smooth L1 loss function was adopted to identify the target signal accurately. This function behaves as a squared loss for small errors to increase sensitivity and as a linear loss for large errors to enhance robustness to outliers. Its mathematical expression is as follows:

$$Loss = \begin{cases} \frac{1}{2}(x_n - y_n)^2, & |x_n - y_n| < 1 \\ |x_n - y_n| - \frac{1}{2}, & |x_n - y_n| \geq 1 \end{cases}, \quad (9)$$

where x_n is the predicted value and y_n is the true value. The model was trained using the Adam optimizer. Figure 4 shows the results of the systematic hyperparameter optimization performed, which lead to the determination of the following optimal training configuration: a batch size of 64, a learning rate of 1×10^{-4}, and an L2 regularization coefficient of 3×10^{-4}. Given the relatively few model parameters and rapid convergence observed, the number of training epochs was set to 50 to prevent overfitting. Finally, the trained DUFC model provides high-quality denoised signals for the subsequent NLS fitting, thereby enabling precise extraction of the ring-down time.

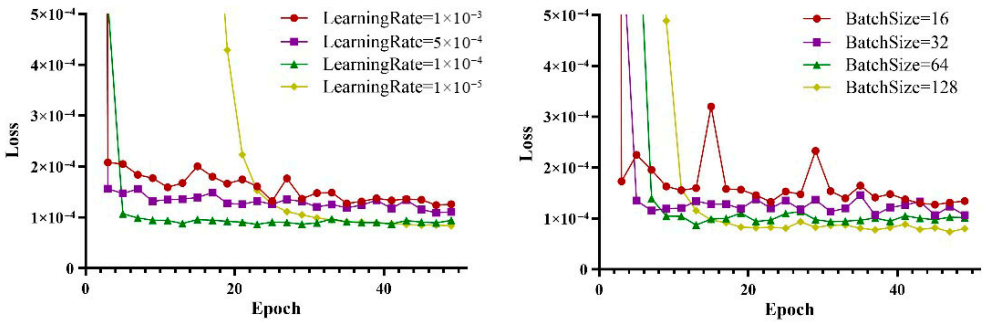

(**a**) (**b**)

Figure 4. Effect of hyperparameter optimization on the model performance: (**a**) effect of the training learning rate and (**b**) effect of the batch size.

3. Results

3.1. Simulation of the Noise Reduction Effect of the Data

In the simulated test dataset, decay curve signals generated from randomly selected ring-down times were chosen as representative samples. The performance of the developed DUFC model was compared with those of traditional time–frequency domain filtering algorithms, such as the Savitzky–Golay (S-G) filter, wavelet transform (WT), and fast Fourier transform (FFT), as well as a multilayer perceptron neural network. For an intuitive comparison, the signal-to-noise ratio (SNR) of the denoised and original smooth signals was used as the evaluation criterion. The SNR is calculated as follows:

$$\mathrm{SNR} = 10 \times \log_{10}\left(\frac{std(Signal_{pure})}{std(Signal_{noise} - Signal_{pure})}\right), \quad (10)$$

where S_{pure} is the pure (noise-free) ring-down signal, S_{noise} is the noisy ring-down signal, and std$(\cdot)$ denotes the standard deviation.

As shown in Figure 5, the average SNR between the noisy data and labels in the training set is 13.86 dB. Among the various traditional and deep learning methods used for denoising, the WT filter, which processes high-frequency coefficients via a direct zero setting, preserves the main signal characteristics well, achieving an average SNR of 18.24 dB. The performance of the S-G filter is highly dependent on the window length and polynomial order. The best filtering result is obtained with an optimal window length of 101 and a polynomial order of 4, yielding an average SNR of 21.52 dB. The polynomial fitting method (degree = 6) smoothens the decay curves by fitting each curve with a high-degree polynomial, which further improves the SNR to 22.67 dB. The support vector machine (SVM) denoising algorithm, which uses a radial basis function kernel with a learning rate of 0.01, achieves an SNR of 21.20 dB when fitting the decay curves. The FFT denoising method, which utilizes mirror padding and a Hamming window to truncate high-frequency components, removes noise rapidly, but results in a relatively low SNR of only 13.67 dB.

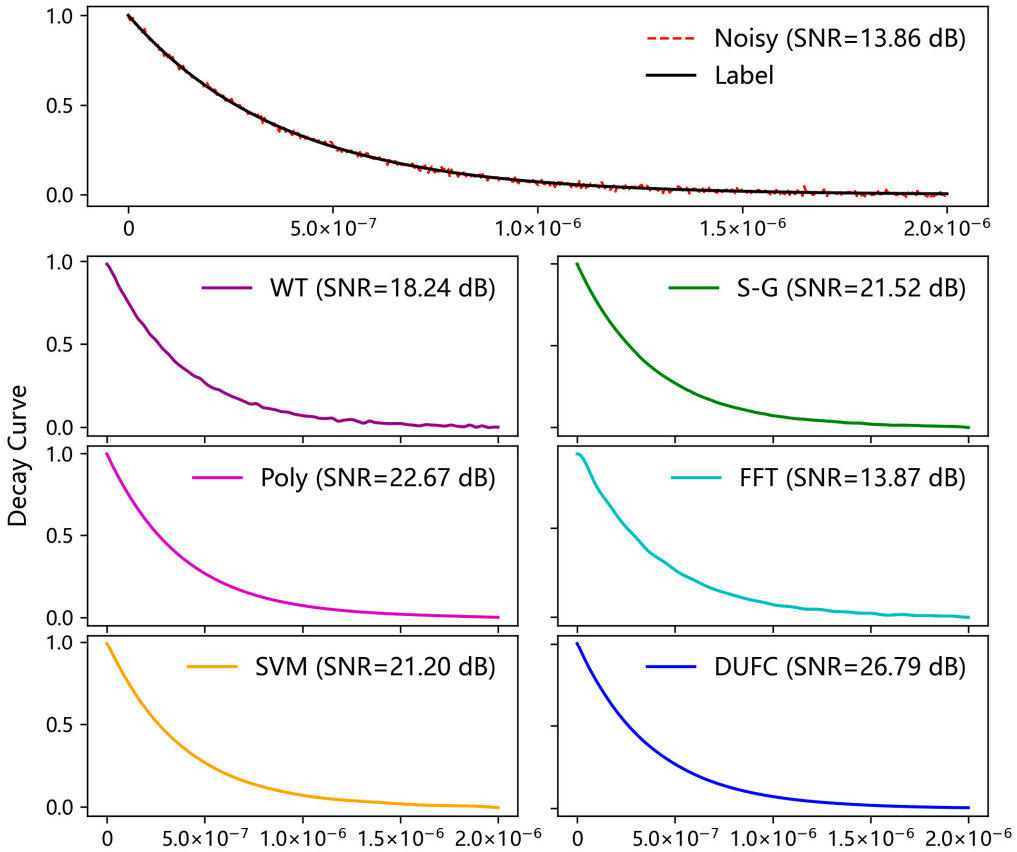

Figure 5. Evaluation of the filtering efficacies of multiple algorithms on simulated noisy decay signals.

By contrast, the DUFC model developed in this study significantly enhances the denoising effect while maintaining the signal fidelity. By processing the decay curves in an end-to-end manner using a deep neural network, the model effectively suppresses high-frequency noise and achieves an SNR of 26.79 dB. This performance is markedly superior to that of the aforementioned traditional methods. Moreover, the DUFC model operates at a very high processing speed, satisfying the real-time requirements for large-scale curve denoising.

The fluctuation amplitude of the residual signal after processing by each algorithm was calculated to evaluate the smoothing and fidelity effects of the different denoising methods on the overall signal, and the results are shown in Figure 6. The WT, S-G, FFT,

and SVM methods exhibit significant fluctuations after denoising. Although these methods can partially eliminate high-frequency interference noise, their ability to suppress low-frequency noise within the signal is limited. The S-G algorithm shows some improvement in handling low-frequency noise; however, its residual remains insufficiently smooth. By contrast, the DUFC algorithm effectively removes low-frequency noise while maximally preserving the detailed characteristics of the signal. Its residual amplitude is the smallest, with a residual standard deviation (STD) of only 5.12×10^{-4}, significantly outperforming the other methods. These results show that the DUFC algorithm can effectively suppress noise in the overall signal while ensuring signal integrity, thereby producing an output signal closer to the theoretically ideal state.

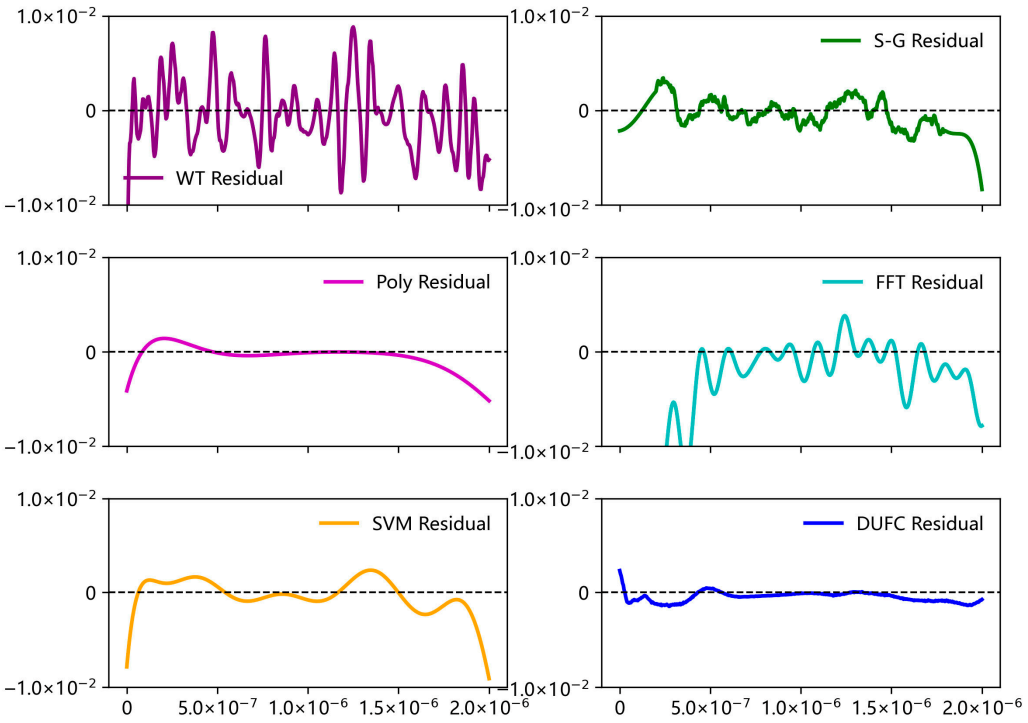

Figure 6. Residual distribution of the denoised curve.

As summarized in Table 3, distinct differences are observed between the processing speed and SNR performance of the algorithms when applied to the 8000 curves in the validation set. Although the FFT method exhibits the highest processing speed (with an average time of 0.000164 s), its average SNR is only 13.72 dB, thereby indicating a limited capacity for noise suppression. The processing speeds of the WT and S-G algorithms are comparable to that of DUFC; however, their average SNRs are 18.38 dB and 20.24 dB, respectively, which are lower than that of DUFC (21.84 dB). This suggests that their denoising effectiveness needs further improvement. The SVM algorithm achieves an average SNR close to that of DUFC but requires a significantly longer processing time (0.057068 s), which makes it less suitable for large-scale data processing. Although polynomial fitting (POLY) achieves a slightly higher average SNR (22.74 dB) than DUFC and reaches a maximum SNR of 30.22 dB, its average processing time is approximately four times that of DUFC, resulting in lower computational efficiency. By contrast, the DUFC algorithm combines high efficiency with excellent denoising capability. It not only achieves an average SNR of 21.84 dB and a maximum SNR of 28.50 dB but also maintains an average processing time of only 0.000207 s, thereby achieving an optimal balance between denoising performance and computational efficiency. These results show that the DUFC algorithm can rapidly

process large-scale curve data while ensuring high signal fidelity, which highlights its practical advantages.

Table 3. Computational efficiency and denoising performance of different algorithms on the validation set.

Algorithm	Average Time Cost/(s)	Average SNR/(dB)	Maximum SNR/(dB)
DUFC	0.000207	21.84	28.50
POLY	0.000818	22.74	30.22
SVM	0.057068	21.95	26.83
FFT	0.000164	13.72	14.52
S-G	0.000283	20.24	24.16
WT	0.000198	18.38	20.08

3.2. Validation Using Experimental Data

To systematically evaluate the performance of the developed DUFC deep learning denoising model within CRDS, six independent repeated measurements were conducted at two noise levels (16 and 128 averages on the oscilloscope) under three conditions: vacuum, ambient air, and 10 ppm standard acetone gas. The results were processed using the linear least squares method, DUFC denoising followed by linear fitting, and the nonlinear least squares method. Analysis was conducted on two main dimensions: intragroup stability and intergroup accuracy.

First, intragroup stability was assessed by calculating the STD of the six repeated τ values within each group to evaluate the robustness of the algorithm to interference. As shown in Figure 7, the DUFC model exhibits superior stability to the other methods under both high-(16 averages) and low-noise (128 averages) conditions. In the low-noise environment baseline with 128 averages, DUFC significantly reduces the STD of τ values from an order of 10^{-8} for the linear method to an order of 10^{-9}. In the high-noise environment with 16 averages, the linear method significantly increases the STD to 4.74×10^{-8}, whereas the DUFC algorithm effectively decreases it to below 2.22×10^{-8}. These results indicate that the DUFC algorithm significantly enhances the repeatability and reliability of measurement outcomes, thereby reducing the reliance on extensive repeated measurements.

Second, an intergroup accuracy analysis was performed to validate the practical value of the algorithm for concentration inversion. Under low-noise conditions (128 averages), the acetone concentrations calculated by the three algorithms were highly consistent (ranging from 8.34 to 8.82 ppm). This confirms that this condition can serve as an evaluation benchmark and that the system itself possesses good inherent accuracy. However, under high-noise conditions (16 averages), the discrepancies between the algorithms were significantly magnified. The concentration calculated using linear fitting exhibited a significant deviation (12.07 ppm, approximately 20.7% error). Although the result from nonlinear fitting (10.42 ppm) showed some improvement, it still contained a notable error. Only the concentration derived from the DUFC denoising algorithm (9.40 ppm) was the closest to the true nominal value. This outcome proves that the DUFC model can optimize the measurement precision of τ values under noise interference and effectively ensures the accuracy and stability of the gas concentration detection results.

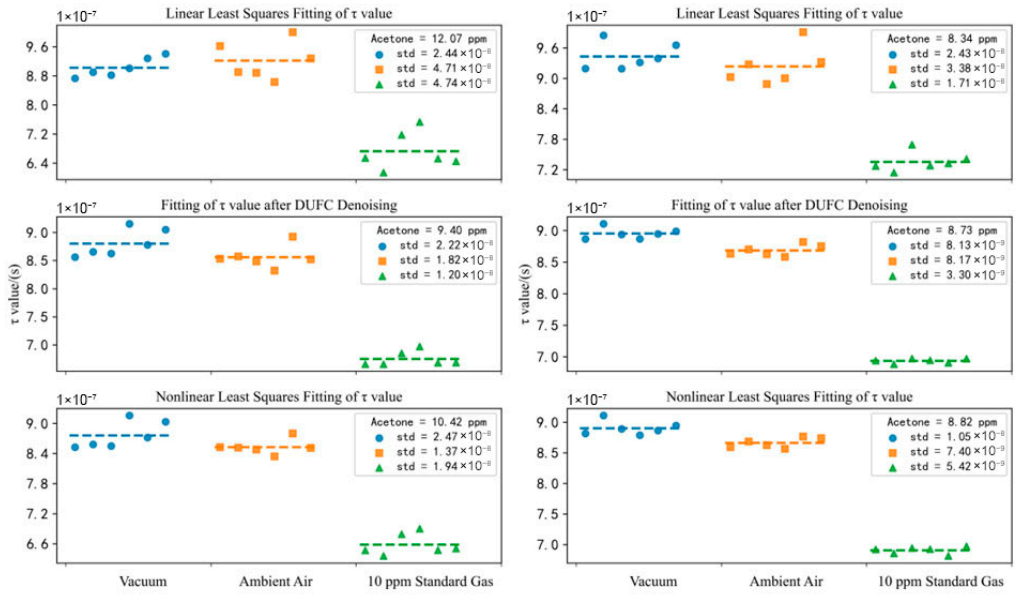

(**a**) (**b**)

Figure 7. Stability of the DUFC algorithm under different noisy conditions: (**a**) analysis of the results for the 16-times averaged signal and (**b**) analysis of the results for the 128-times averaged signal.

4. Discussion

This study addressed the problems of strong noise interference and insufficient stability for ring-down-time extraction by CRDS-based breath acetone detection systems. A deep learning-based denoising approach for ring-down curves, called DUFC, was developed. Unlike conventional filtering and fitting techniques, DUFC learns the intrinsic structures of ring-down signals in the feature space, thereby enabling effective separation of signals and noise while avoiding significant waveform distortion.

In terms of denoising performance, DUFC increased the SNR of the simulated ring-down curves from 13.86 dB to 26.79 dB, which was markedly higher than that achieved by polynomial fitting (22.67 dB) and FFT-based filtering (13.72 dB). Moreover, the residual STD was reduced to 5.12×10^{-4}, which indicated that DUFC effectively suppressed noise while preserving the physical characteristics of the original decay signal. These results suggest that DUFC is not merely a smoothing or frequency-domain truncation method but rather a data-driven modeling approach for the ring-down process.

Regarding computational efficiency, the average processing time for a single ring-down curve using DUFC was only 0.000207 s, which was comparable to that of the FFT method and significantly shorter than that of the polynomial and nonlinear least-squares fitting methods. This indicates that despite the introduction of a neural network, DUFC retains strong potential for real-time processing by meeting the high-speed data processing requirements of CRDS detection systems.

Experimental validation further showed the robustness and stability of the DUFC model. Under high-noise conditions, the intragroup STD of the extracted ring-down time τ was reduced from 4.74×10^{-8} using linear fitting to 2.22×10^{-8} using DUFC, indicating a substantial improvement in the extraction consistency. At the highest noise level, the acetone concentration retrieved by DUFC was the closest to the true value (10 ppm), which was better than linear fitting (12.07 ppm) and nonlinear fitting (10.42 ppm), thereby confirming its reliability under extreme measurement conditions.

Overall, DUFC exhibits advantages in terms of the denoising performance, computational efficiency, and stability, and offers an effective data-driven solution for high-precision ring-down time extraction using CRDS gas detection systems.

5. Conclusions

A deep learning-based denoising method for CRDS ring-down curves called DUFC was developed to improve the accuracy and stability of ring-down time extraction in breath acetone detection. Both simulation and experimental results showed that DUFC outperforms conventional filtering and fitting methods in terms of the SNR improvement, residual suppression, and extraction consistency while maintaining a computational efficiency comparable to that of FFT-based approaches. The method remained reliable under high-noise conditions and enabled the accurate retrieval of acetone concentrations, thereby indicating strong robustness and practical applicability. This study offers an effective signal processing solution for CRDS-based noninvasive glucose monitoring. Future studies should focus on lightweight network designs and embedded implementations to facilitate portable and real-time applications.

Author Contributions: Conceptualization, C.J. and J.S.; methodology, W.L., D.S. and F.W.; software, W.L. and Y.S.; validation, W.L., D.S. and F.W.; formal analysis, D.S. and F.W.; investigation, W.L., D.S., F.W. and Y.Y.; resources, C.J. and J.S.; data curation, W.L., D.S. and Y.Y.; writing—original draft preparation, W.L. and D.S.; writing—review and editing, C.J. and J.S.; visualization, W.L., D.S., F.W. and Y.Y.; supervision, Y.S.; project administration, C.J. and J.S.; funding acquisition, C.J. All authors have read and agreed to the published version of the manuscript.

Funding: This research was funded by the National Key Research and Development Program of China (Grant No. 2022YFC2406204), Taishan Industrial Leadership Talent Project (Grant No. tscx202306125), Shandong Provincial Key Research and Development Program (Grant Nos. 2023CXPT041 and 2024CXPT054), Jinan Social and Livelihood Project of Shandong Province, and Qingdao Science and Technology Benefiting the People Project (Grant No. 25-1-5-smjk-5-nsh). The APC was funded by the authors.

Institutional Review Board Statement: Not applicable.

Informed Consent Statement: Not applicable.

Data Availability Statement: The data presented in this paper were generated using numerical simulations based on the mathematical models and parameters described in the manuscript. No additional datasets were generated or analyzed. These data can be reproduced using the equations and methods presented in this article.

Conflicts of Interest: Authors Feifei Wang, Yuxiao Song and Yong Yang were employed by the company Jinan Guoke Medical Technology Development Co., Ltd. The remaining authors declare that the research was conducted in the absence of any commercial or financial relationships that could be construed as a potential conflict of interest.

Abbreviations

The following abbreviations are used in this manuscript:

CRDS	Cavity Ring-Down Spectroscopy
PMT	Photomultiplier Tube
SNR	Signal-to-Noise Ratio
DUFC	Decay-Upsampling FC-Net
FFT	Fast Fourier Transform
WT	Wavelet Transform
NLS	Nonlinear Least Squares

References

1. Berden, G.; Peeters, R.; Meijer, G. Cavity Ring-down Spectroscopy: Experimental Schemes and Applications. *Int. Rev. Phys. Chem.* **2000**, *19*, 565–607. [CrossRef]
2. Li, J.; Guo, B.; Sun, X.; Wang, K.; Yang, H. Current Pulse Width Modulation-Cavity Ring down Spectroscopy for Simultaneous Measurement of Carbon Dioxide and Methane. *Sens. Actuators B Chem.* **2025**, *444*, 138457. [CrossRef]
3. Amann, A.; Costello, B.D.L.; Miekisch, W.; Schubert, J.; Buszewski, B.; Pleil, J.; Ratcliffe, N.; Risby, T. The Human Volatilome: Volatile Organic Compounds (VOCs) in Exhaled Breath, Skin Emanations, Urine, Feces and Saliva. *J. Breath Res.* **2014**, *8*, 034001. [CrossRef] [PubMed]
4. Liu, H.; Liu, W.; Sun, C.; Huang, W.; Cui, X. A Review of Non-Invasive Blood Glucose Monitoring through Breath Acetone and Body Surface. *Sens. Actuators Phys.* **2024**, *374*, 115500. [CrossRef]
5. Arbia, M.B.; Kim, S.-H.; Yoon, J.-B.; Comini, E. Preparation of NiO NWs by Thermal Oxidation for Highly Selective Gas-Sensing Applications. *Sensors* **2025**, *25*, 2075. [CrossRef] [PubMed]
6. Gashimova, E.; Osipova, A.; Temerdashev, A.; Porkhanov, V.; Polyakov, I.; Perunov, D.; Dmitrieva, E. Exhaled Breath Analysis Using GC-MS and an Electronic Nose for Lung Cancer Diagnostics. *Anal. Methods* **2021**, *13*, 4793–4804. [CrossRef] [PubMed]
7. Anderson, J.C. Measuring Breath Acetone for Monitoring Fat Loss: Review. *Obesity* **2015**, *23*, 2327–2334. [CrossRef] [PubMed]
8. Yu, T.; Meng, X.; Hao, X.; Dong, Z.; Wang, Y.; Sun, S.; Cheng, P. YSZ-Based Mixed-Potential Acetone Sensor with LaBaCo2O5+δ Sensitive Electrode for Diabetic Diagnosis. *Sens. Actuators B Chem.* **2024**, *418*, 136273. [CrossRef]
9. Long, D.A.; Fleisher, A.J.; Wójtewicz, S.; Hodges, J.T. Quantum-Noise-Limited Cavity Ring-down Spectroscopy. *Appl. Phys. B* **2014**, *115*, 149–153. [CrossRef]
10. Hashiguchi, K.; Amano, M.; Cygan, A.; Lisak, D.; Ciuryło, R.; Abe, H. Improvement of the Cavity in CRDS for High-Precision Measurement of Trace Moisture. *AIP Conf. Proc.* **2024**, *3230*, 140004. [CrossRef]
11. Wang, D.; Hu, R.-Z.; Xie, P.-H.; Qin, M.; Ling, L.-Y.; Duan, J. Fast and Accurate Extraction of Ring-Down Time in Cavity Ring-Down Spectroscopy. *Spectrosc. Spect. Anal.* **2014**, *34*, 2845–2850.
12. Zhang, D.; Wang, H.; Feng, Y.; Wang, X.; Liu, G.; Han, K.; Gong, X.; Liu, J.; Zhan, X.; Chen, J. Fast Fourier Transform (FFT) Using Flash Arrays for Noise Signal Processing. *IEEE Electron. Device Lett.* **2022**, *43*, 1207–1210. [CrossRef]
13. Zhang, G.; Hao, H.; Wang, Y.; Jiang, Y.; Shi, J.; Yu, J.; Cui, X.; Li, J.; Zhou, S.; Yu, B. Optimized Adaptive Savitzky-Golay Filtering Algorithm Based on Deep Learning Network for Absorption Spectroscopy. *Spectrochim. Acta A Mol. Biomol. Spectrosc.* **2021**, *263*, 120187. [CrossRef] [PubMed]
14. Liu, G.; Chen, X.; Zhang, Y.; Liang, H. Spectral Denoising Approach Using Enhanced Wavelet Packet-Optimized EEMD Algorithm. *Vib. Spectrosc.* **2025**, *140*, 103844. [CrossRef]
15. Tu, Y.; Lin, Y.; Zha, H.; Zhang, J.; Wang, Y.; Gui, G.; Mao, S. Large-Scale Real-World Radio Signal Recognition with Deep Learning. *Chin. J. Aeronaut.* **2022**, *35*, 35–48. [CrossRef]
16. França, R.P.; Borges Monteiro, A.C.; Arthur, R.; Iano, Y. An Overview of Deep Learning in Big Data, Image, and Signal Processing in the Modern Digital Age. In *Trends in Deep Learning Methodologies*; Elsevier: Amsterdam, The Netherlands, 2021; pp. 63–87. ISBN 978-0-12-822226-3.
17. Jiang, Y.; Li, H.; Rangaswamy, M. Deep Learning Denoising Based Line Spectral Estimation. *IEEE Signal Process. Lett.* **2019**, *26*, 1573–1577. [CrossRef]
18. Kistenev, Y.V.; Skiba, V.E.; Prischepa, V.V.; Borisov, A.V.; Vrazhnov, D.A. Gas-Mixture IR Absorption Spectra Denoising Using Deep Learning. *J. Quant. Spectrosc. Radiat. Transf.* **2024**, *313*, 108825. [CrossRef]
19. Wu, S.; Zhang, Y.; He, C.; Luo, Z.; Chen, Z.; Ye, J. Self-Supervised Learning for Generic Raman Spectrum Denoising. *Anal. Chem.* **2024**, *96*, 17476–17485. [CrossRef] [PubMed]
20. Lai, Z.; Yan, C.; Fu, Y. Hybrid Spectral Denoising Transformer with Guided Attention. In Proceedings of the 2023 IEEE/CVF International Conference on Computer Vision (ICCV), Paris, France, 1–6 October 2023; pp. 13019–13029. [CrossRef]
21. Parson, W.W.; Burda, C. *Modern Optical Spectroscopy: From Fundamentals to Applications in Chemistry, Biochemistry and Biophysics*; Springer: Berlin/Heidelberg, Germany, 2016.

Disclaimer/Publisher's Note: The statements, opinions and data contained in all publications are solely those of the individual author(s) and contributor(s) and not of MDPI and/or the editor(s). MDPI and/or the editor(s) disclaim responsibility for any injury to people or property resulting from any ideas, methods, instructions or products referred to in the content.